ICAS-96-1.6.3

AN ANALYSIS OF VORTEX BREAKDOWN PREDICTED BY THE EULER EQUATIONS

D. Strohmeyer, M. Orlowski, J.M.A. Longo
Institute of Design Aerodynamics, DLR Braunschweig, Fed. Rep. of Germany

D. Hummel, A. Bergmann
Institute of Fluid Mechanics, Technical University Braunschweig, Fed. Rep. of Germany

Abstract

In the present paper a numerical / experimental investigation is presented to address the ability of the solution of the Euler equations to describe spiral-type vortex breakdown for sharp-edged delta wings. The configuration selected is a 65° swept, cropped delta wing with and without canard. The investigation is carried out at $M_\infty = 0.2$ for two angles of attack, $\alpha = 10°$ and 20°. The experimental results include water and wind tunnel flow investigations, while the numerical study is carried out with the CEVCATS code using a structured grid with about 1 million points. The influence of artificial viscosity and grid topology on the numerical solution is investigated. Although the implemented numerical scheme is formulated to provide steady-state solutions and hence not time accurate, the results clearly demonstrate the ability of this technique to describe spiral-type vortex breakdown. All essential experimental findings known until now have been closely reproduced.

Nomenclature

C_D	drag coefficient
C_L	lift coefficient
c_p	pressure coefficient
$c_{p,\,tot.}$	total pressure coefficient, $c_{p,\,tot.} = (p_{tot.}-p_\infty) / q_\infty$
i, j, k	grid index system (Fig. 2)
$k^{(4)}$	damping coefficient [21]
M	Mach number
MC	multigrid cycle, time step
p	static pressure
q	dynamic pressure
Re	Reynolds number, based on root chord length
T	local turbulence level (Eq. 4)
t	time
U	velocity, $U = ((u^2+v^2+w^2) / 3)^{0.5}$
u, v, w	velocity components
x, y, z	cartesian coordinate system in streamwise, spanwise and vertical direction, origin at wing apex
α	angle of attack
φ, γ	transformation angles between vortex-fixed and cartesian coordinate system (Fig. 4)
ρ	density
$\| \partial\rho/\partial t \|$	density residual
ξ, η, ζ	cartesian coordinate system, non-dimensionalized by root chord length
η', ζ'	local cartesian coordinate system, non-dimensionalized by local half-span

Superscript

-	mean value (Eq. 1)
'	standard deviation (Eq. 2)
*	experimental fluctuation

Subscript

C	canard
max.	maximum value
min.	minimum value
v	vortex fixed
W	wing
∞	free stream value

1. Introduction

Vortex flows associated with separation from leading edges play an important role in todays high-angle-of-attack aerodynamics. The efforts of industry to increase the performance and manoeuvrability of modern fighter as well as supersonic transport aircraft result in slender wings with sharp leading edges. At high angles of attack these wings generate significant forces through a complex system of vortices which is caused by the rolling-up of the shear layer leaving the leading edge. The forces could be exploited to aerodynamic advantage as long as the vortices are stable and symmetric, but this is limited by the onset of vortex breakdown [1, 2]. This phenomenon produces large, abrupt changes in forces and moments jeopardizing flight safety. The prevention of vortex breakdown and hence the possibility of improvements in the performance can be reached by careful generation and control of the system of vortices.

Experimental investigations show that the fundamental structure of the vortices is insensitive to the Reynolds number since the flow is dominated by the vortices and they are embedded in an essentially irrotational field [3]. Sharp leading edges guarantee the fixed location of the primary separation and high Reynolds numbers reduce the influence of secondary separations on the primary vortex. Experimental investigations show also that the onset of vortex breakdown is less influenced by viscous effects but by pressure gradients [4-6].

For the mentioned geometries and flow conditions CFD research has produced a number of methods based on approaches from linearized potential formulations [7] to the Reynolds-averaged Navier-Stokes equations [8-12], where vortices evolve as part of the solution. While the first category of methods is restricted to linear problems and the location of vortices must be known a priori, the latter leads to high computational costs and exhibits the lack of a suitable general turbulence model. Methods based on the Euler equations, without the specification of an explicit Kutta condition to enforce separation, are able to simulate vortex sheets from the leading edge as well [13-15]. Their computational costs are not as high, but they neglect viscous effects. Nevertheless, they might be economical tools to provide an insight into the system of vortices over slender wings, especially for industrial purposes.

The ability of methods based on the Euler equations to simulate the phenomenon of vortex breakdown has been reported in several papers [16-18]. However, a detailed analysis of the type of vortex breakdown described by this numerical simulation - i.e. bubble or spiral - is missing in the literature. The present paper focuses on the analysis of vortex breakdown described by the solution of the Euler equations. After a description of the studied configurations as well as the boundary conditions of the experimental and numerical simulations, the essential results of the simulation are presented.

2. Methodology

2.1 Configurations

For the investigation of the vortex breakdown phenomenon the geometry of the International Vortex Flow Experiment (IVFE) [15, 19] with and without canard was chosen. Between the experimental configurations exist geometric differences concerning the leading edge and the fuselage, listed in Tab. 1. While these differences may affect the position of the leading edge vortex, their influence on the breakdown phenomenon can be neglected as the outline-shape of wing and canard remains the same. Figure 1 illustrates the geometric parameters of the experimental configurations by means of the canard-on wind tunnel model. In the numerical simulation both configurations, with and without canard, do not include a fuselage but only sharp edged wing and canard geometry in coplanar arrangement.

configuration	leading edge	fuselage crossection	wing section	application
canard-off	sharp	rectangular	flat plate	water tunnel • flow visualization[26]
canard-off	sharp	rectangular	IVFE	wind tunnel • probe measurements[19,26]
canard-on	sharp	rectangular	IVFE	water tunnel • flow visualization[26]
canard-on	sharp	rectangular	IVFE	wind tunnel, $\alpha = 10°$ • probe measurements[19,26]
canard-on	round	circular, below wing	IVFE	wind tunnel, $\alpha = 20°$ • LDV measurements[25]

Tab. 1 Experimental configurations.

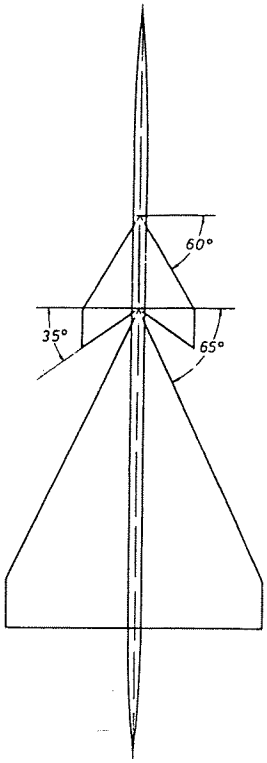

Geometric Parameters

Canard

Aspect Ratio	$\Lambda_C = 1.65$
Taper Ratio	$\lambda_C = 0.4$
Sweep L. Edge	$\varphi_{CLE} = 60°$
Sweep T. Edge	$\varphi_{CTE} = 35°$
Rel. Thickness	$t_C = 0.05$

Wing

Aspect Ratio	$\Lambda_W = 1.38$
Taper Ratio	$\lambda_W = 0.15$
Sweep L. Edge	$\varphi_{WLE} = 65°$
Sweep T. Edge	$\varphi_{WTE} = 0°$
Rel. Thickness	$t_W = 0.05$

Combination	coplanar
Span Ratio	$b_C / b_W = 0.44$

Fig. 1 Geometric parameters of the canard-on wind tunnel model.

2.2 Experimental Investigation

The experimental studies include wind tunnel measurements as well as water tunnel investigations. They were carried out at the Institute of Fluid Mechanics at Technical University Braunschweig.

The water tunnel experiments are used for flow visualization at Re = 7500. The wind tunnel tests have been performed in the 1.3 m wind tunnel ('Göttingen-type', open testsection). Three-component and flow field measurements with a conical 5-hole-probe have been carried out at $M_\infty = 0.1$ and $Re = 1.4 \times 10^6$ for different angles of attack.

LDV measurements at Re = 0.5 x 10^6 are provided in different planes perpendicular to the symmetry plane.

2.3 Numerical Simulation

The numerical simulation is based on the solution of the three dimensional, compressible Euler equations in integral form using the DLR Euler code CEVCATS [20]. The spatial discretization of the solution algorithm is characterized by a cell vertex scheme and central differences. For the damping of numerical oscillations first and third order dissipative terms are added to the governing equations, following Jameson et al. [21]. In subsonic flow the artificial viscosity is decisively controlled by the user-defined damping coefficient $k^{(4)}$. The larger the coefficient, the smaller is the dissipation. Its influence on the the vortex breakdown simulation has been investigated in the present work. For the integration of the resulting system of ordinary differential equations in time, an explicit five-stage Runge-Kutta scheme is applied, making use of three techniques to accelerate the convergence to a steady state: local time stepping, implicit smoothing of the residual and a multigrid method.

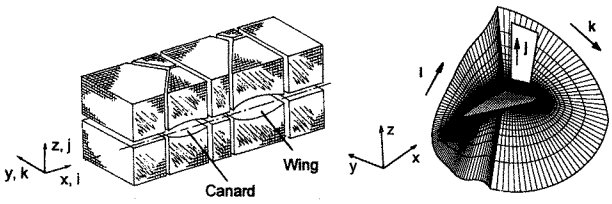

Fig. 2 Grid with H-H topology (left) and C-O topology (right).

For the calculations an algebraic grid with about 1 million points arranged in a 14-block H-H topology was generated (Fig. 2). The flowfield above the canard is discretized with 25 x 65 x 49 points in streamwise (i-), normal (j) and spanwise (k-) direction. Each of the two blocks following in streamwise direction - between wing and canard as well as above the wing - consists of 49 x 65 x 49 points. Further characteristics of the grid are the farfield boundary extension of approximately 2 wing chord lengths in all directions and a minimum spacing normal to canard and wing at the trailing edge of 0.001 wing chord lengths. For the canard-off configuration the same grid was used, removing the block of the canard. In order to study the influence of the grid structure, i.e. grid topology and distribution of points, a second grid was generated for the canard-off configuration, using a 1-block C-O topology with 113 x 73 x 129 points in i, j, and k-direction (Fig. 2). The distance between body and farfield is extended to approximately 10 wing chord lengths. Compared with the H-H topology the grid clustering in vertical direction is reduced, leading to a more even distribution of grid points and therefore to a better resolution of the vortex core. Due to this procedure the minimum spacing normal to the wing in the grid plane at the trailing edge is enlarged to 0.004 wing chord lengths. A comparison of the grid stucture in a vertical plane at the wing trailing edge is given in Fig. 3.

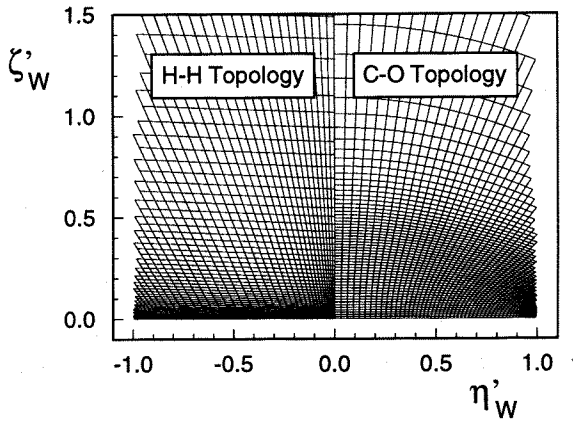

Fig. 3 Grid structure in the vertical plane at the trailing edge, $\xi = 1.0$.

In general two criteria are applied for the assessment of the convergence of numerical solutions: the drop of the density residual and the behavior of the lift coefficient. In this study a steady-state solution was considered as being converged if the residual dropped at least three orders of magnitude and the lift coefficient was fixed up to 4 decimal places. The demand on the lift coefficient is significantly higher compared to general engineering applications. It is wellknown that in the case of vortex breakdown above slender wings the numerical solution does not converge to a steady state. For these unsteady solutions the demand of a harmonic oscillation of the lift coefficient in time was used as convergence criterion in addition to the drop of the density residual. The reason for that will be given in the discussion of the results.

In order to estimate the steadiness of the flowfield mean values and standard deviations of the flow variables were calculated for a period of multigrid cycles, MC_1 ... MC_2. This evaluation is based on the following definitions of mean value and standard deviation, illustrated by means of the density ρ in the gridpoint i, j, k:

mean value

$$\bar{\rho}_{i,j,k} = \frac{1}{MC_2 - MC_1 + 1} \sum_{t = MC_1}^{MC_2} \rho_{i,j,k,t} \qquad (1)$$

standard deviation

$$\rho'_{i,j,k} = \sqrt{\frac{1}{MC_2 - MC_1} \sum_{t = MC_1}^{MC_2} (\rho_{i,j,k,t} - \bar{\rho}_{i,j,k})^2} \quad . \qquad (2)$$

For unsteady solutions, where the lift coefficient did not converge to a steady value, the number of multigrid cycles under consideration was fixed to one period of the C_L-oscillation. For steady-state solutions the same number was chosen.

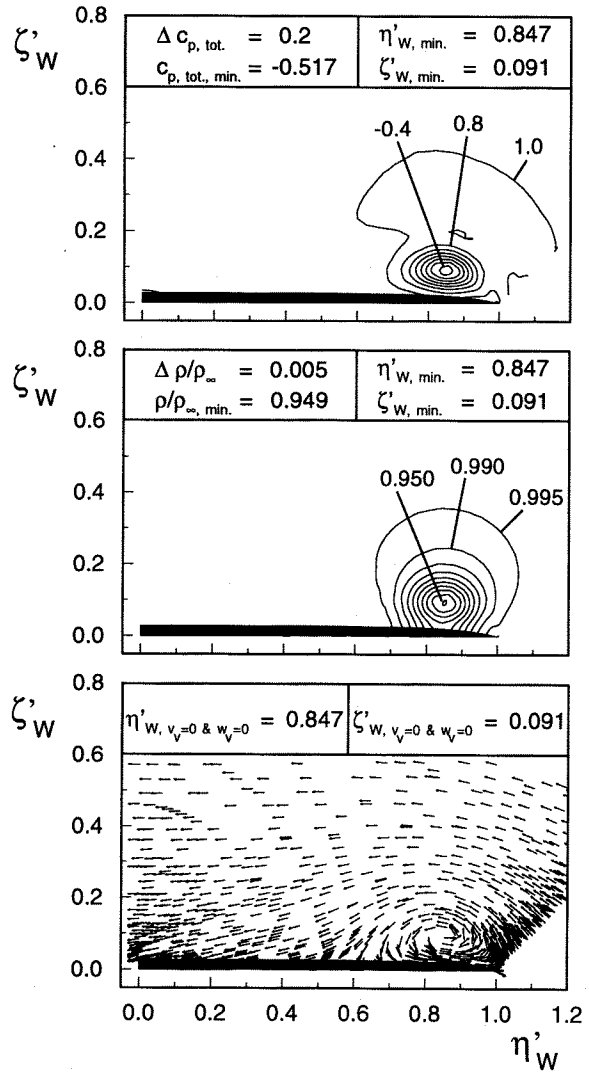

Fig. 4 Total pressure coefficient (above), density (middle) and cross components of the velocity (below) for the canard-off configuration at $\xi = 0.8$, $\alpha = 10°$ and $M_\infty = 0.2$.

In the flowfield analysis the minimum of the total pressure coefficient in a vertical plane ξ = const. was chosen as criterion for the location of the vortex axis. For the description of the spatial structure of the vortex axis iso-surfaces of the total pressure coefficient were used. The criterion for the vortex axis was derived from a detailed analysis of vortical flow with and without vortex breakdown. The numerical simulations showed a perfect agreement of the local minima of the scalar variables total pressure, static pressure and density in streamwise direction and the location of points in the vortex flow having only a velocity component in the direction of the vortex axis u_v but no cross components in a vortex-fixed coordinate system $v_v = w_v = 0$. Figure 4 illustrates this relation for the canard-off configuration at $\alpha = 10°$ in the cross section $\xi = 0.8$. For the determination of the points with no cross components of the velocity the vortex-fixed coordinate system was introduced according to Fig. 5 and the velocity components transformed into this system corresponding to the transformation angles φ and γ:

$$\begin{bmatrix} u_v \\ v_v \\ w_v \end{bmatrix} = \begin{bmatrix} \cos\varphi\cos\gamma & \sin\varphi\cos\gamma & \sin\gamma \\ -\sin\varphi & \cos\varphi & 0 \\ -\cos\varphi\sin\gamma & -\sin\varphi\sin\gamma & \cos\gamma \end{bmatrix} \cdot \begin{bmatrix} u \\ v \\ w \end{bmatrix} \quad . \qquad (3)$$

Once the vortex bursts and reverse flow occurs the directions of the local vortex-fixed coordinate system were extrapolated in streamwise direction.

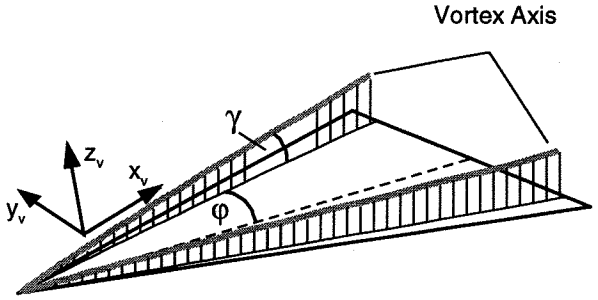

Fig. 5 Vortex-fixed coordinate system.

The validation of the CEVCATS code with respect to the simulation of seperated flows has been documented in several publications [18, 22, 23]. A typical convergence history is given in Fig. 6 for the canard-off configuration at $\alpha = 10°$ and $M_\infty = 0.2$, showing a steady-state solution.

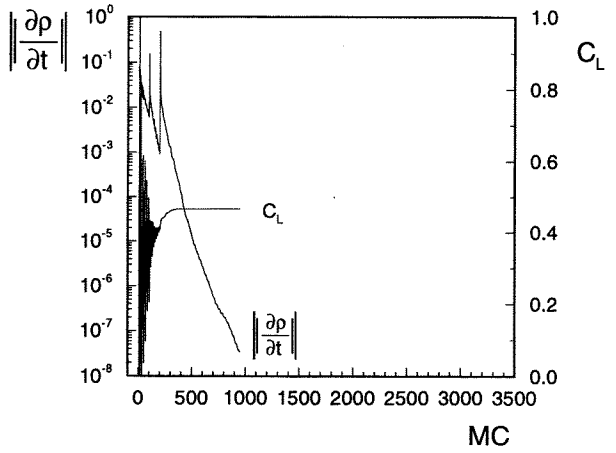

Fig. 6 Convergence history for the canard-off configuration, $\alpha = 10°$ and $M_\infty = 0.2$.

A comparison of the calculated flowfield with experimental results in terms of the static pressure (Fig. 7) shows a good qualitative and quantitative correlation between ex-

periment and numerical simulation. Shape and location of the leading edge vortex compare quite well. For the canard-on configuration the same quality of the numerical result compared with the experimental measurements has been obtained as illustrated in Fig. 8 for the static pressure coefficient. The existing quantitative discrepancies are due to viscous effects and a loss of numerical resolution at the canard itself.

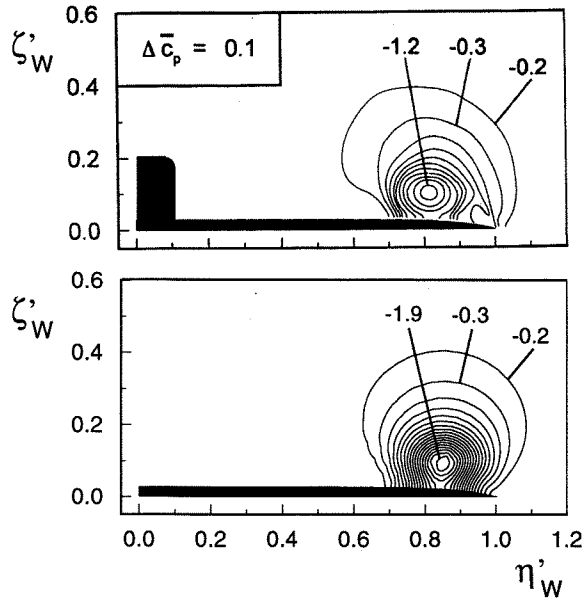

Fig. 7 Mean pressure coefficient for the canard-off configuration at $\xi = 0.8$, $\alpha = 10°$ and $M_\infty = 0.2$. Experiment [26] (above) and numerical simulation (below).

In addition the calculated $\alpha = 10°$-solution for both configurations has been analysed with respect to the standard deviation of the flow quantities. The level of the standard deviation of this converged steady-state solutions can be considered as a measure for the fluctuations resulting exclusively from the numerical procedure. The knowledge of this 'numerical noise' is necessary for the evaluation of an unsteady solution where the higher standard deviation of the flow quantities is based on physical phenomena. It is obvious that for a steady-state solution the level of the standard deviation depends on the convergence level of the solution in terms of the density residual: The deeper the density residual has dropped, the lower is the level of the standard deviation of the flow quantities. In Fig. 9 the standard deviation of the pressure coefficient for the canard-off configuration is shown in a vertical plane at $\xi = 0.8$. It has been calculated for an intervall of 30 multigrid cycles at the end of the solution process (MC = 921 ... 950) where the density residual is of the order $\| \partial\rho/\partial t \| = 1 \times 10^{-7}$ (Fig. 6). The standard deviation of this highly converged solution is random distributed and, with the maximum value $c_p'_{max.} = 1.6 \times 10^{-6}$, at least 5 orders of magnitude below the mean values (Fig. 7). An analogous result has been obtained for the canard-on configuration.

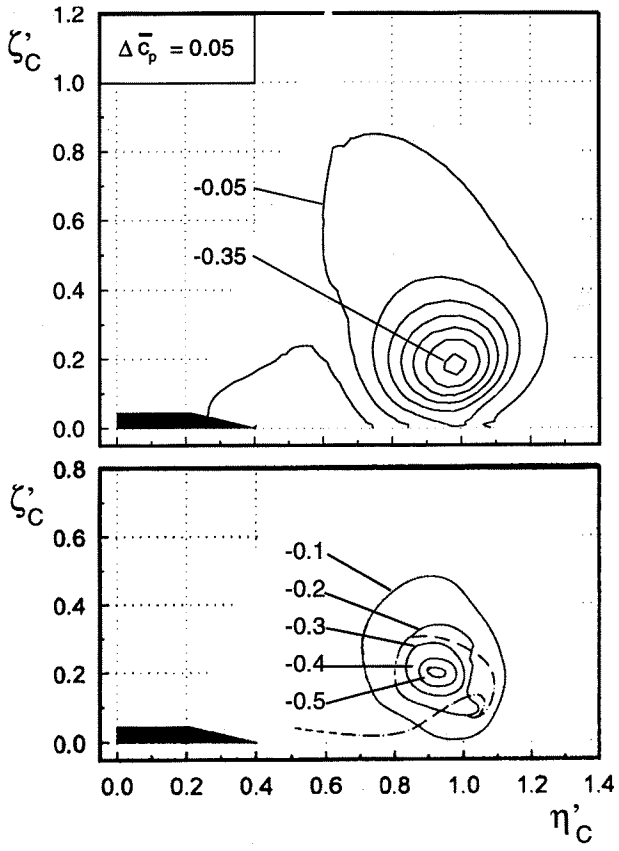

Fig. 8 Mean pressure coefficient for the canard-on configuration at $\xi = 0.15$, $\alpha = 10°$ and $M_\infty = 0.2$. Numerical simulation (above) and experiment [26] (below).

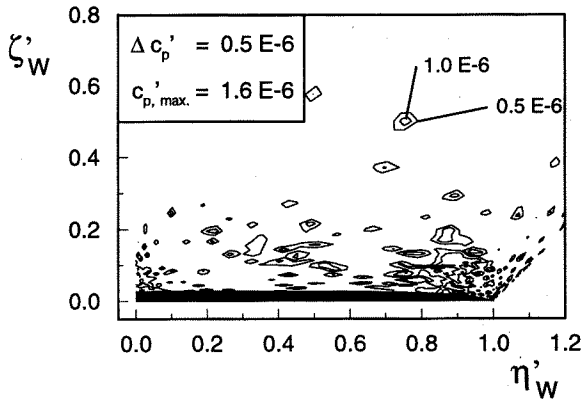

Fig. 9 Standard deviation of the calculated pressure coefficient for the canard-off configuration at $\xi = 0.8$, $\alpha = 10°$ and $M_\infty = 0.2$.

3. Results

3.1 Vortex Breakdown

The vortex breakdown over the canard-off configuration has been investigated at $\alpha = 20°$ and $M_\infty = 0.2$ on the H-H grid. For this angle of attack the Euler code does not converge to a steady state according to Fig. 10. After a drop of 3 orders of magnitude the residual remains almost constant and the lift coefficient shows oscillations. At the end of 1000 multigrid cycles it oscillates harmonicly with an amplitude of about 1.5% of the mean value $C_L = 0.955$ and a period of 30 multigrid cycles.

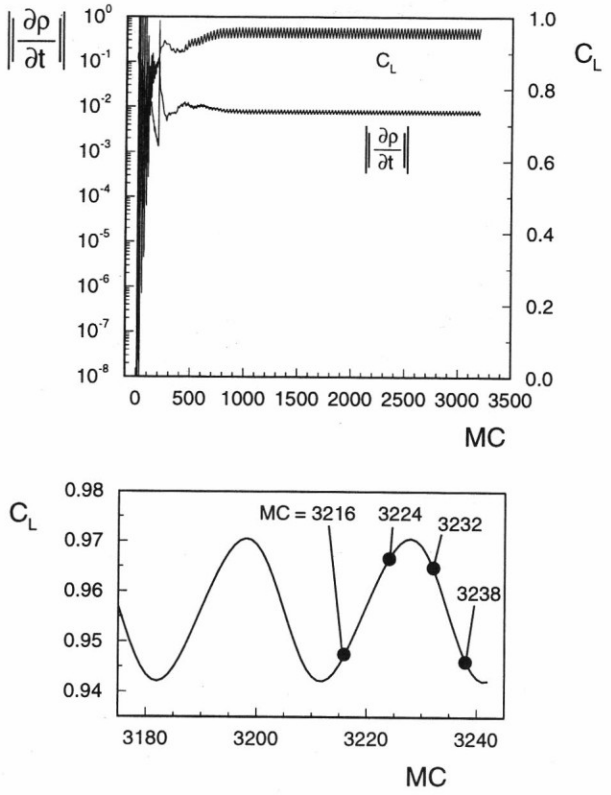

Fig. 10 Convergence history for the canard-off configuration and detail, $\alpha = 20°$ and $M_\infty = 0.2$.

The surface pressure distribution as calculated on the H-H grid is shown in Fig. 11. The mean values on the left-hand side indicate the well-known vortex pattern. The corresponding standard deviation is shown on the right-hand side. Compared to the steady $\alpha = 10°$–case in Fig. 9 the values have increased of about 5 orders of magnitude. This indicates an unsteady flow situation within the vortex close to the trailing edge. The values of the standard deviation reach a maximum there and fade away in upstream direction.

The further analysis of the unsteady phenomena is carried out in two steps: In the first place the flow is analysed in space for a fixed time step (MC = 3216). The result is shown in Fig. 12. A region of reverse flow is found close to the wing trailing edge, indicated by the iso-surface $u_v = 0$. The vortex axis, visualized by an iso-surface of the total pressure coefficient, turns out to be a straight line in streamwise direction starting from the wing apex. In the vicinity of the reverse flow region the vortex axis moves downwards and inboard, thus forming a spiral with a sense of rotation against that of the vortex, see also Fig. 16. This means that for the time step under consideration the structure of the vortex is of spiral type.

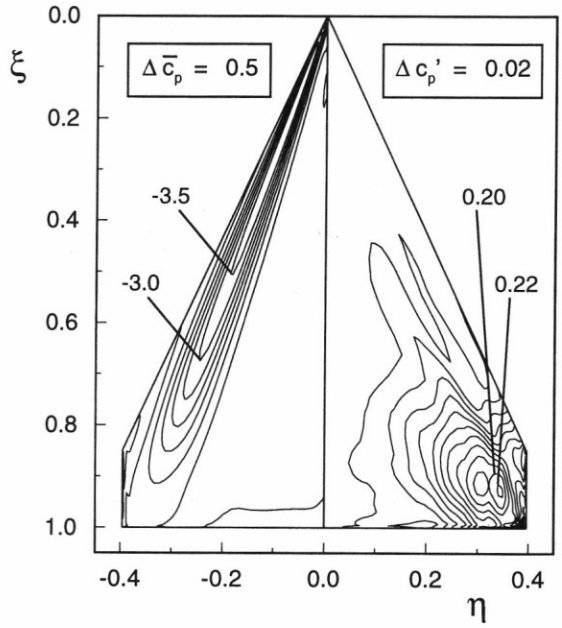

Fig. 11 Surface pressure coefficient calculated on the H-H grid at $\alpha = 20°$ and $M_\infty = 0.2$. Mean value (left) and standard deviation (right).

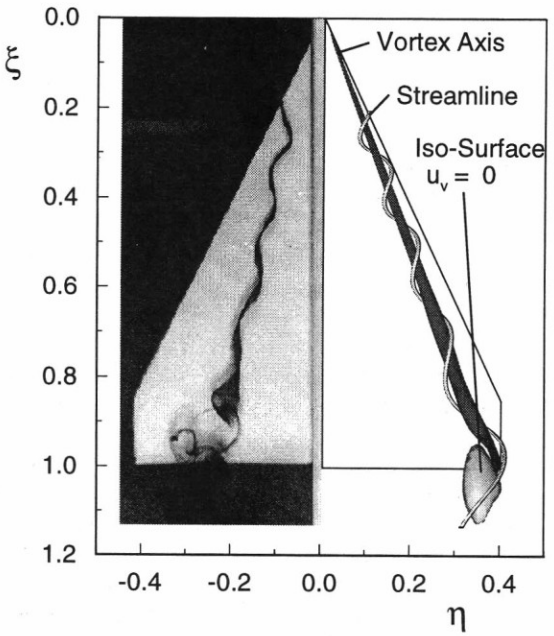

Fig. 12 Flow visualization at $\alpha = 20°$. Experiment [26] (left) and numerical simulation for MC = 3216 (right).

In a second step the flowfield is analysed for different time steps (MC = 3216, 3224, 3232 and 3238) at a fixed location. As a result the distribution of the total pressure coefficient is given in the plane $\xi = 0.99$ close to the trailing edge (Fig. 13). The vortex axis is indicated by the minimum of the total pressure coefficient. It turns out that, with respect to time, the spiral-shape part of the vortex axis rotates in the sense of the vortex motion.

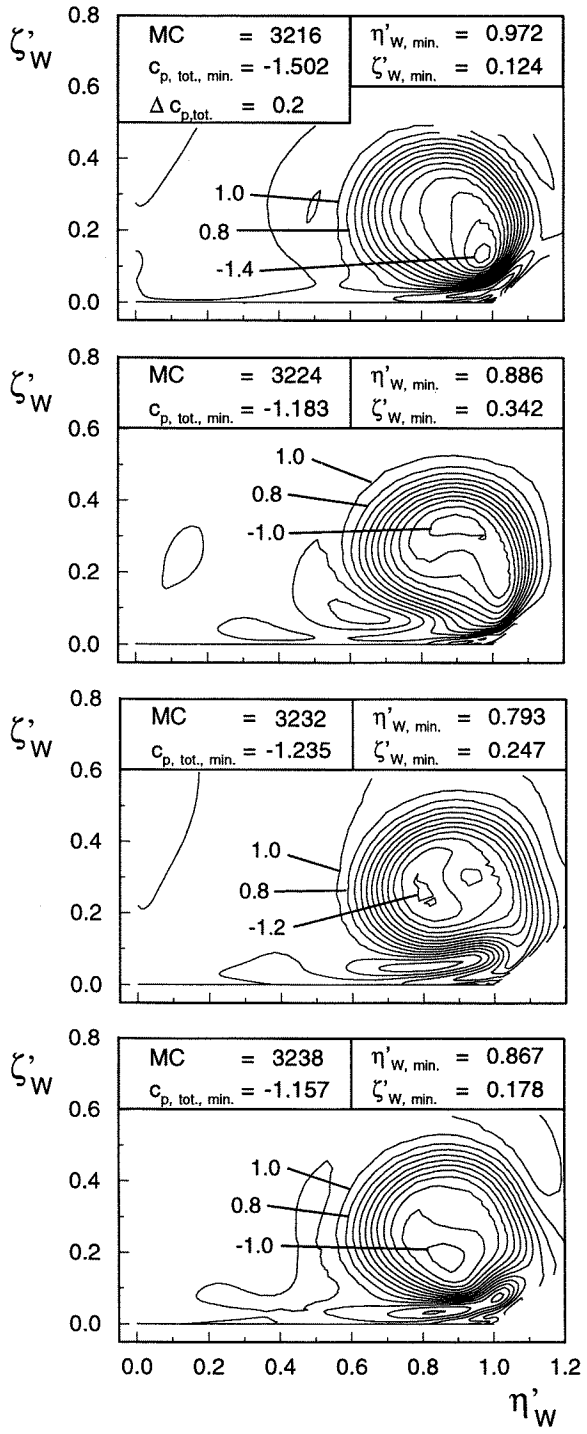

Fig. 13 Total pressure coefficient for the canard-off configuration at $\xi = 0.99$, $\alpha = 20°$ and $M_\infty = 0.2$.

In Fig. 14 a vertical plane through the vortex axis (in the region $0 \le \xi \le 0.8$) is considered showing the standard deviation of the total pressure coefficient. A funnel-shape structure with isolated maximum values can be observed. This structure results from the rotating motion of the vortex axis. Hence, the periodic rotation of the vortex axis in the breakdown region causes strong fluctuations of the flow quantities which also influence the flow on the wing surface and lead to the significant oscillations of the aerodynamic coefficients mentioned above.

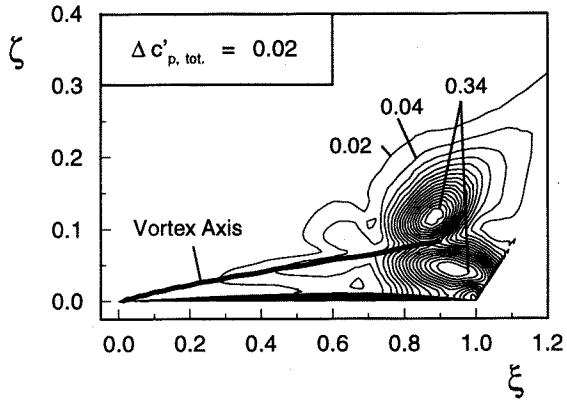

Fig. 14 Standard deviation of the calculated total pressure coefficient for the canard-off configuration in a vertical plane along the vortex axis, $\alpha = 20°$ and $M_\infty = 0.2$.

The numerical results of the present analysis are in excellent agreement with all existing observations of spiral-type vortex breakdown in experiments. Figure 12 shows e.g. the flow visualization in the water tunnel with spiral-type vortex breakdown close to the wing trailing edge.

The influence of artificial viscosity and of grid topology on the spiral-type vortex breakdown has been investigated. All the results for the canard-off configuration discussed above have been obtained on the H-H grid with a damping coefficient $k^{(4)} = 16$. Further calculations with $k^{(4)} = 12$, 32 and 128 have been carried out (Fig 15). The convergence history for $k^{(4)} = 12$ and 32 shows a behavior as for $k^{(4)} = 16$ according to Fig. 10. Moreover both calculations describe qualitatively the same solution, a spiral-type vortex breakdown as discussed previously. The quantitative differences result from the influence of the artificial viscosity: The higher the artificial viscosity, the more the vortex flow is damped, leading to smaller gradients of the flow quantities, smaller deviations and consequently a smaller amplitude of the C_L-oscillation. However flowfield analyses showed almost identical size and position of the reverse flow region for $k^{(4)} = 12$, 16 and 32. On the other hand, if the reduction of the artificial viscosity reaches a certain level, the harmonic C_L-oscillation is superimposed by additional disturbances as indicated for $k^{(4)} = 128$ in Fig. 15. In this case the standard deviation level

of the flow quantities increases significantly and the spiral-type breakdown structure can no longer be identified. These results justify the applied convergence criterion of harmonic oscillation of the lift coefficient (see section 2.3) for converged solutions. The effect of the artificial viscosity on the occurrence and identification of spiral-type vortex breakdown can be summarized as follows: Usual values of the damping coefficient $k^{(4)} = 12, 16, 32$ which provide convergence for steady-state solutions ($\alpha = 10°$) cover also the spiral-type vortex breakdown ($\alpha = 20°$). For larger values of $k^{(4)}$ convergence to a steady state as well as to an unsteady state is lost. The beginning of this process can be seen for $k^{(4)} = 128$ in Fig. 15.

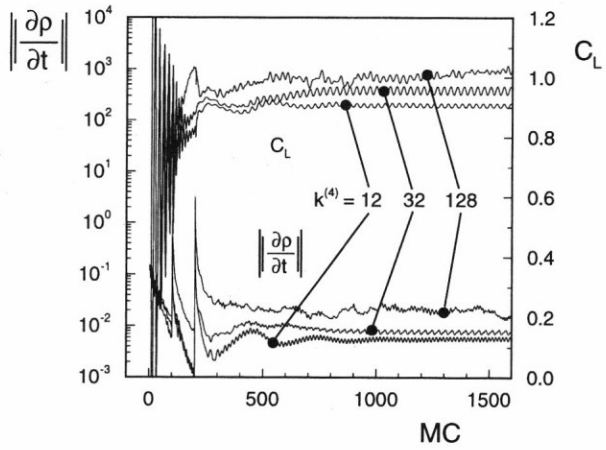

Fig. 15 Convergence history for the canard-off configuration with different artificial viscosity, $\alpha = 20°$ and $M_\infty = 0.2$.

Finally the spiral-type vortex breakdown has been calculated by means of another grid topology. For this purpose a C-O grid was used with about the same total number of grid points as in the previous investigations. Nevertheless the vortex flowfield in the vicinity of the wing is covered by a larger number of grid points leading to a better resolution of the flowfield as indicated in Fig. 3. The damping coefficient was $k^{(4)} = 32$. In spite of the different grid structure the calculation converged to almost the same oscillating solution as obtained previously on the H-H grid: The location of the vortex axis as well as size and position of the reverse flow region are the same, as shown in Fig. 16 for a certain time step. The vortex axis is marked by an iso-surface of the total pressure coefficient. In the vortex breakdown region the vortex axis winds around the reverse flow region against the sense of the vortex flow motion as already shown in Fig. 12. The surface pressure distribution calculated on the C-O grid for $\alpha = 20°$ is shown in Fig. 17 for comparison with the corresponding result of the H-H grid in Fig. 11. The surface pressure mean values are about the same. However, high values of the standard deviation are not only observed in the breakdown region but also more upstream where the H-H grid solution exhibited steady flow. An analysis of several time steps showed that the increase of the standard deviation upstream of the vortex breakdown results from the rotation of a slightly deformed vortex axis in this region. This phenomenon is also known from experimental investigations [24]. In detail the spatial amplitude in the region upstream of vortex breakdown is significantly smaller compared to that in the breakdown region, but the gradients of the flow quantities are much stronger there which causes the high fluctuations. Hence, the better resolution of the vortex flow on the C-O grid provides more detailed information about the vortex breakdown phenomenon.

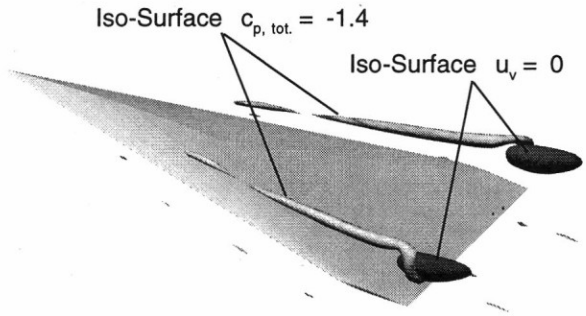

Fig. 16 Vortex axis and reverse flow calculated on the C-O grid for a fixed time step, $\alpha = 20°$ and $M_\infty = 0.2$.

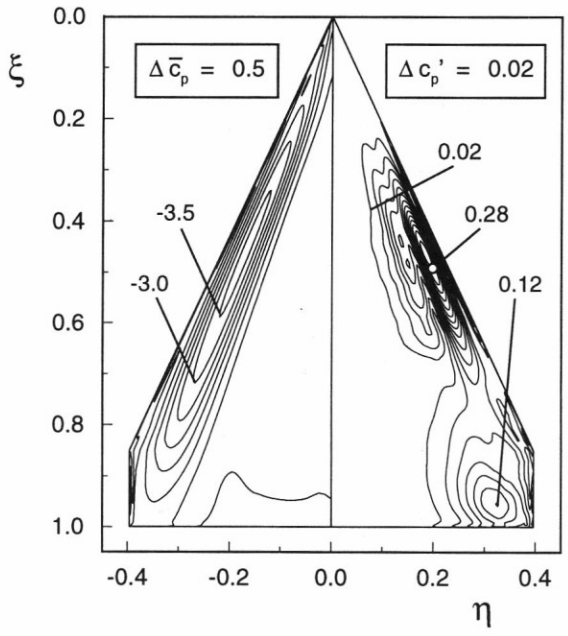

Fig. 17 Surface pressure coefficient calculated on the C-O grid at $\alpha = 20°$ and $M_\infty = 0.2$. Mean value (left) and standard deviation (right).

3.2 Vortex Stretching

Experimental investigations on close-coupled canard configurations [25, 26] have shown vortex stretching phenomena in the region between canard and wing. In order to understand this process in more detail, Euler calculations have been carried out for the IVFE canard-on configuration at $\alpha = 20°$ and $M_\infty = 0.2$. The results are compared with wind tunnel LDV measurements. Figure 18 presents the measured mean velocity in horizontal sections through the canard vortex axis in the region between the canard and the wing.

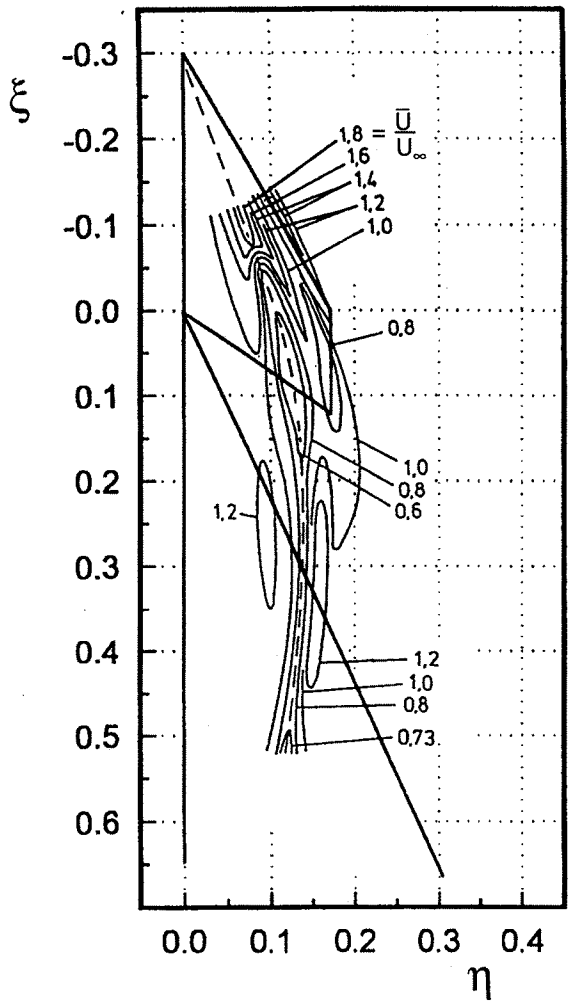

Fig. 18 LDV measurements [25] of the velocity in sections through the canard vortex at $\alpha = 20°$.

In the centre of the vortex the flow is decelerated near the canard trailing edge and re-accelerated close to the wing leading edge. In the present wind tunnel investigation the axial velocity along the vortex axis is positive everywhere, but water tunnel flow visualizations have also shown reverse flow in this region. From the LDV experiments a measure for the experimental fluctuations can be derived. For this purpose a local turbulence level T has been determined:

$$T = \frac{1}{\bar{U}} \cdot \sqrt{\frac{\overline{u^{*2}} + \overline{w^{*2}}}{2}} \quad , \qquad (4)$$

which is based on the fluctuation of two velocity components u* and w* and on the local mean velocity $\bar{U}$. Figure 19 shows the results in horizontal sections through the canard vortex axis. The fluctuations increase close to the trailing edge of the canard and decrease near the leading edge of the wing. Hence, between canard and wing reduced velocities and increased fluctuations are present within the canard vortex. This phenomenon is also clearly indicated in the flow visualization from water tunnel experiments according to Fig. 20.

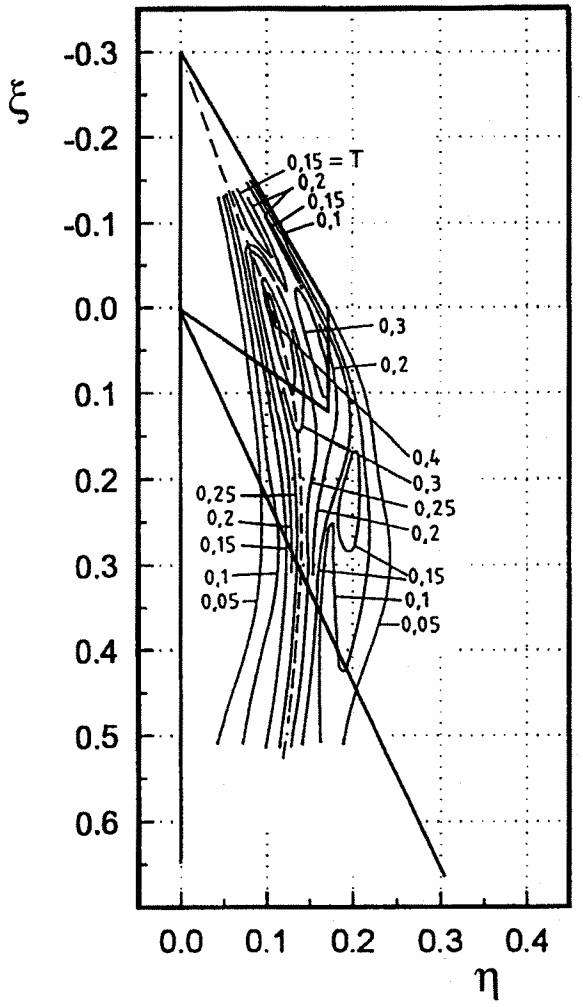

Fig. 19 Local turbulence level in sections through the canard vortex, results of LDV measurements [25] at $\alpha = 20°$.

The numerical simulation for the canard-on configuration converged smoothly, similar to the $\alpha = 10°$-case of the canard-off and the canard-on configuration as discussed in section 2.3. Furthermore, this computation has been repeated for different damping coefficients $k^{(4)} = 32, 64$ as well as 128 and the results do not indicate any significant differences.

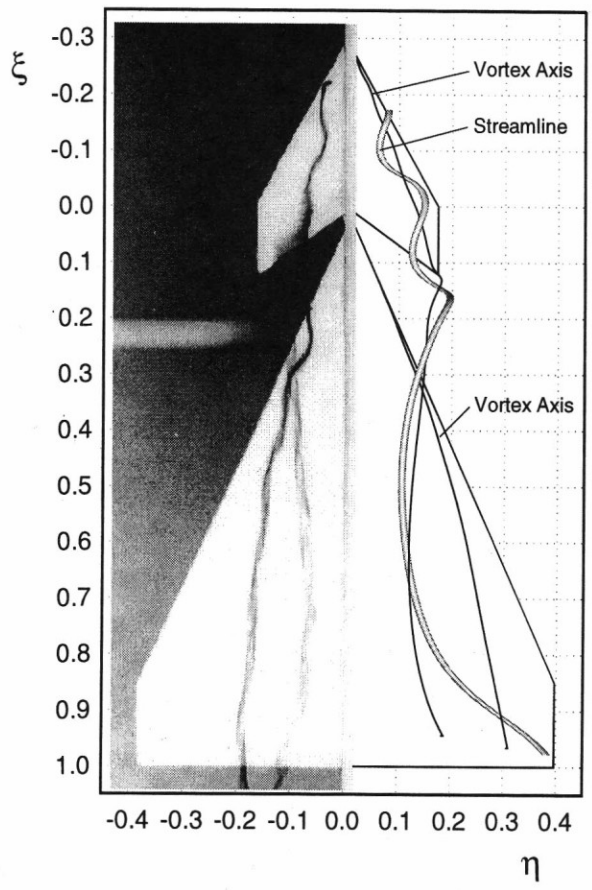

Fig. 20 Flow visualization at $\alpha = 20°$. Experiment [26] (left) and numerical simulation (right).

The structure of the flowfield is analysed in Fig. 21 by a comparison of calculated and measured velocities in a cross section at $\xi = 0.05$ through the centre of the stretching region. Both results show a region of reduced velocities near the vortex axis which is surrounded by an annular region of higher velocities. The flow phenomena are the same in the experiment and the numerical simulation and the values of the extrema correlate quite well. Concerning the location of the canard vortex axis considerable differences between the experimental and numerical result are present due to the fact that viscosity effects such as the secondary separation are not taken into account and due to differences in geometry.

Using the techniques described in section 2.3 the location of the axis of the canard vortex and of the wing vortex has been evaluated and plotted in Fig. 20. In addition a certain streamline of the canard vortex is shown. The stretching process takes place over the rear part of the canard and downstream of the canard trailing edge. In this region the vortex axis shows a remarkable kink towards the symmetry plane and upwards. For $M_\infty = 0.20$ a region of reverse flow could not be detected, but this matter is very sensitive to the free stream Mach number, since for $M_\infty = 0.21$ a small region of reverse flow is present. The general flow pattern of the numerical simulation correspond to the water tunnel flow visualization which is shown on the left-hand side of Fig. 20. Compared to the wind tunnel and the numerical results the flow visualization in the water tunnel shows that the location of the canard vortex is shifted towards the symmetry plane due to the significantly lower Reynolds number of the water tunnel experiment.

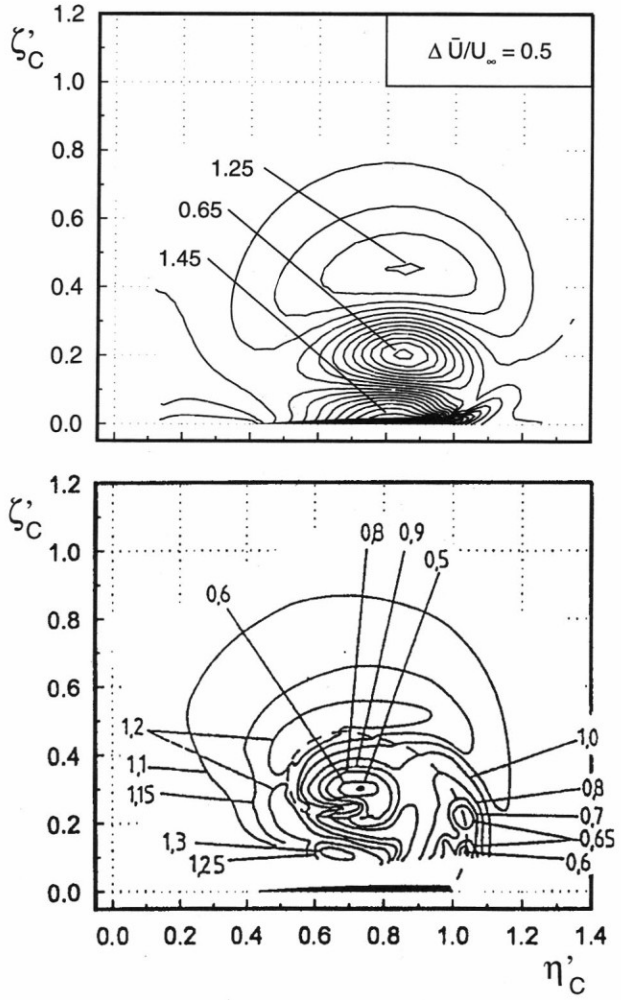

Fig. 21 Mean velocity for the canard-on configuration at $\xi = 0.05$, $\alpha = 20°$ and $M_\infty = 0.2$. Numerical simulation (above) and experiment [25] (below).

In Fig. 22 the calculated standard deviation of the axial velocity in a plane through the canard vortex axis in the stretching region is shown. The observed values are about 4 orders of magnitude higher than those of the $\alpha = 10°$-solution. Hence, the level of the standard deviation is one order of magnitude below the level observed in connection with spiral-type vortex breakdown. In detail a spiral structure of the vortex axis could not be identified. The high values of the standard deviation result from a bulging and stretching of the decelerated flow.

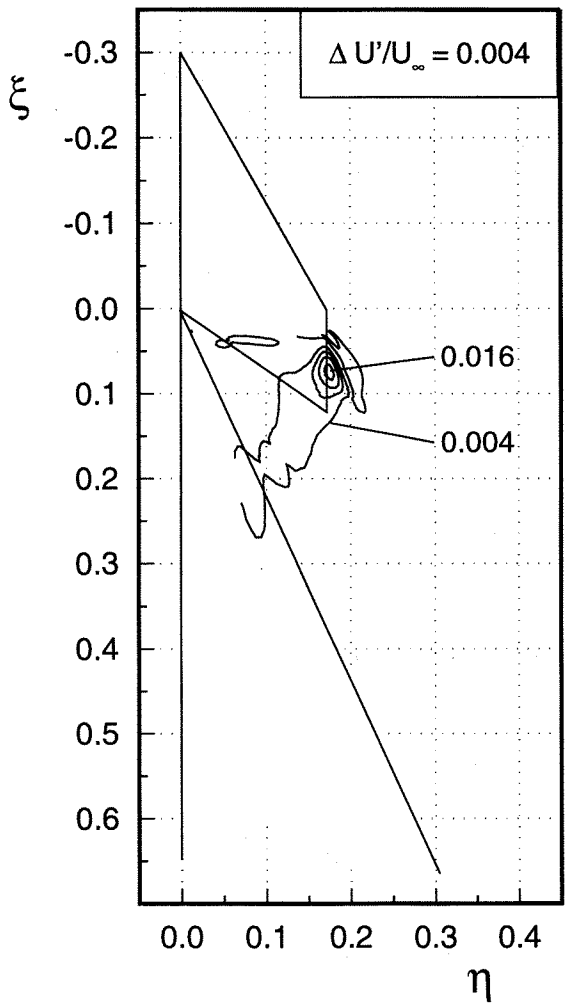

Fig. 22 Standard deviation of the calculated axial velocity component in a plane through the core of the canard vortex, $\alpha = 20°$ and $M_\infty = 0.2$.

According to all the described features of the vortex stretching, this phenomenon can be considered as a rearrangement of the vortex structure and hence it might be seen as a preliminary condition necessary for the development of vortex breakdown.

4. Final Remarks

An analysis was presented on the delta wing vortex breakdown predicted by the numerical solution of the Euler equations, using a numerical scheme implemented for steady-state solutions. The study was carried out using the DLR computer code CEVCATS and the low speed test facilities of TU Braunschweig. The incompressible flow ($M_\infty = 0.2$) around a 65° swept, cropped delta wing with and without a close-coupled canard was studied for two angles of attack, $\alpha = 10°$ and 20°. The experimental investigations of the vortex flow included LDV and probe measurements as well as water tunnel flow visualizations.

The numerical simulation was carried out on a structured grid of about 1 million grid points. The accuracy of the computer solutions was addressed by sensitivity studies concerning variations of numerical parameters and grid topology.

For the canard-off configuration, the investigations showed an unsteady behavior of the numerical solution once vortex breakdown occurs, leading to periodic oscillations of the aerodynamic forces. For a fixed time the spatial distribution of the flow quantities indicates a spiral structure of the vortex axis in the breakdown region, which is well-known from experiments. When time proceeds the spiral structure rotates in the sense of the vortex motion. This periodic rotation leads to the observed oscillations of the flow quantities. In the breakdown region reduced axial velocities as well as reverse flow was found.

For the canard-on configuration the numerical solution did not exhibit wing vortex breakdown but a stretching of the canard vortex in the region between the canard trailing edge and the wing leading edge. While the axial velocity component showed an abrupt deceleration in this region, leading to reverse flow in some cases, no spiral structure of the vortex axis could be identified.

Concluding, despite the lack of time accuracy the numerical solution predicted many of the important flow features associated with vortex breakdown.

5. References

1. Hummel, D., "On the Vortex Formation over a Slender Delta Wing at Large Angles of Attack", AGARD CP-247, 1978, pp. 15-1 to 15-17.

2. Erickson, G.E., "Vortex Flow Correlation", ICAS Paper 82-6.6.1, 13th International Council of the Aeronautical Sciences, Sept. 1982.

3. Payne, F.M., Ng, T.T., Nelson, R.C., Schiff, L.B., "Visualization and Flow Surveys of the Leading Edge Vortex Structure on Delta Wing Planforms", AIAA Paper 86-330, 1986.

4. Ludwieg, H., "Experimentelle Nachprüfung der Stabilitätstheorien für reibungsfreie Strömungen mit schraubenlinienförmigen Stromlinien", *Zeitschrift für Flugwissenschaften und Weltraumforschung*, Vol. 12, 1964, pp. 304 - 309.

5. Stahl, W., Hartmann, K., Schneider, W., "Force and Pressure Measurements on a Slender Delta Wing at Transonic Speed and Varying Reynolds Numbers", AGARD CP-83, 1971, pp. 9-1 to 9-12.

6. Schrader, K.F., Reynolds, G.A., Novak, C.J., "Effects of Mach Number and Reynolds Number on Leading Edge Vortices at High Angle of Attack", AIAA Paper 88-0122, 1988.

7. Hoeijmakers, H.W.M., "Computational Vortex Flow Aerodynamics", AGARD CP-342, 1983, pp. 18-1 to 18-35.

8. Thomas, J.L., Newsome, R.W., "Navier-Stokes Computation of Lee-Side Flows over Delta Wings", AIAA Paper 86-1049, 1986.

9. Kandil, O.A., Chuang, A.H., Shifflette, J.M., "Finite-Volume Euler and Navier-Stokes Solvers for Three Dimensional and Conical Vortex Flows over Delta Wings", AIAA Paper 87-0041, 1987.

10. Fujii, K.J., Schiff, L.B., "Numerical Simulation of Vortical Flows over a Strake Delta Wing", AIAA Paper 87-1229, 1987.

11. Longo, J.M.A., "Simulation of Complex Inviscid and Viscous Vortex Flow", IUTAM *Symposium on Fluid Dynamics of High Angle of Attack*, edited by R. Kawamura and Y. Aihara, Springer-Verlag, Berlin, 1993, pp. 363 - 373.

12. Visbal, M.R., "Structure of Vortex Breakdown on a Pitching Delta Wing", AIAA Paper 93-0434, 1993.

13. Hitzel, S.M., Schmidt, W., "Slender Wings with Leading-Edge Vortex Separation - a Challenge for Panel-Methods and Euler-Codes", AIAA Paper 83-0262, 1983.

14. Murman, E., Rizzi, A., "Applications of Euler Equations to Sharp Edge Delta Wings with Leading Edge Vortices", AGARD CP-412, 1986, pp. 15-1 to 15-22.

15. "Symposium on International Vortex Flow Experiment on Euler Code Validation", Elsenaar, A., Eriksson, G. (Eds.), Proceeding of the Symposium, Stockholm, 1986.

16. O'Neil, P.J., Barnett, R.M., Louie, C.M., "Numerical Simulation of Leading Edge Vortex Breakdown using an Euler Code", AIAA Paper 89-2189, 1989.

17. Mondiano, D.L., Murmann, E.M., "Adaptive Computations of Flow around a Delta Wing with Vortex Breakdown", AIAA Paper 93-3400, 1993.

18. Das, A., Longo, J.M.A., "Numerical Analysis of the Vortical Flow around a Delta Wing-Canard Configuration", *Journal of Aircraft*, Vol. 32, 1995, pp. 716 - 725.

19. Hummel, D., Oelker, H.-C., "Low Speed Characteristics for the Wing-Canard Configuration of the International Vortex Flow Experiment", *Journal of Aircraft*, Vol. 31, No. 4, 1994, pp. 868 - 878.

20. Kroll, N., Radespiel, R., Rossow, C.C., "Accurate and Efficient Flow Solvers for 3D Applications on Structured Meshes", VKI Lecture Serie *Computational Fluid Dynamics*, Brussels, 1994.

21. Jameson, A., Schmidt, W., Turkel, E., "Numerical Solution of the Euler Equations by Finite Volume Methods Using Runge-Kutta Time Stepping Schemes", AIAA-Paper 81-1259, 1981.

22. Longo, J.M.A., Das, A., "Numerical Simulation of Vortical Flows over Close-Coupled Canard-Wing Configurations", AIAA Paper 90-3003, 1990.

23. Longo, J.M.A., "Compressible Inviscid Vortex Flow of a Sharp Edged Delta Wing", *AIAA Journal*, Vol. 33, No. 4, 1995, pp. 680 - 686.

24. Staufenbiel, R., Helmig, T., Vitting, T., "Controlled Breakdown of Tip Vortices", Proceeding of Colloquium on Vortex Breakdown, BBC Baden, 1987, pp. 95 - 114.

25. Bergmann, A., Hummel, D., "Wirbelstruktur zwischen Leitwerk und Flügel an einer Entenkonfiguration", Proceeding des 8. DGLR-Fach-Symposiums, Köln, 1992, pp. 145 - 149.

26. Oelker, H.-C., Aerodynamische Untersuchungen an kurzgekoppelten Entenkonfigurationen bei symmetrischer Anströmung", Zentrum für Luft- und Raumfahrttechnik, Technische Universität Braunschweig, Fed. Rep. Germany, ZLR-Forschungsbericht 90-01, 1990.